# Control of multimodal topological edge modes in magnetoelastic lattices

Taehwa Lee[1,*,‡] Bertin Many Manda[2,‡] Xiaopeng Li[1] Ziqi Yu[1] Georgios Theocharis[2] and Chiara Daraio[3,†]

[1]*Toyota Research Institute of North America, Toyota Motor North America, Ann Arbor, Michigan 48105, USA*

[2]*Laboratoire d'Acoustique de l'Université du Mans (LAUM), UMR 6613, Institut d'Acoustique - Graduate School (IA-GS), CNRS, Le Mans Université, Le Mans, France*

[3]*Division of Engineering and Applied Science, California Institute of Technology, Pasadena, California 91125, USA*

One-dimensional topological acoustic systems offer robust signal transmission and localization in compact spaces. Here, we demonstrate the ability to control both longitudinal and transverse topological waves in a quasi-one-dimensional elastic lattice, composed of an array of repelling magnets connected to elastic cantilevers. The two different topological modes can be separately or simultaneously excited at selected frequencies. Our system enables controlled multimodal propagation and edge localization, owing to its finite size and to the design of longitudinal and transverse topological band gaps within similar frequency ranges. In addition to the robustness of the topological modes to unintentional disorder, we show that disorder can couple degrees of freedom and tailor the energy distribution between longitudinal and transverse waves. This system may enable other studies on the interactions of topological modes useful in sensing and information-processing applications.

## I. INTRODUCTION

The use of topological acoustic systems offers opportunities for alternative functionalities, like time-varying, cross-frequency operation, mode and frequency conversion, and signal-to-noise ratio enhancement, in devices with a smaller footprint for sensing and rf applications. In particular, one-dimensional (1D) topological systems, with broadband operation and a small footprint, are desirable in information processing, due to their robust propagation and localization of waves [1,2] and their simpler integration with other components, such as transducers, resonators, and waveguides [3]. Extraordinary topological features have been demonstrated in various systems, including photonic devices [4], and acoustic and elastic devices [5,6]. However, 1D topological insulators face the challenge of limited propagation modes, which reduce the channels for information processing, when compared to their higher-dimensional counterparts.

A promising solution proposed to increase the functionalities of low-dimensional systems involves introducing synthetic dimensions [7–10], which permit access to higher-dimensional physics in lower-dimensional systems

[9]. For instance, by adding a time modulation to a 1D topological insulator, can allow the observation of topological wave transport otherwise accessible starting from two-dimensional (2D) topological systems [11]. However, this approach requires precise control over the system's internal or external degrees of freedom (DOF) [7,8] to achieve other topological states, band structures, and transport properties, often requiring the use of active components [12–14]. Harnessing tunability in acoustic devices also broadens their potential for applications. This has been demonstrated in various tunable systems [15–18]. Although tunability allows for a synergistic combination with topological physics [19–26], it increases the system's complexity.

Elastic lattices with magnetic coupling have emerged as attractive platforms to study theoretically and experimentally nonlinearity [27–29], long-range interactions [30], tunability [31,32], energy harvesting [33], and time-modulated nonreciprocity [34], in discrete, finite systems. Such discrete systems and their models provide elegant platforms for the exploration of complex wave phenomena [35–38], including the control of topological phases. Despite their versatility, however, magnetically coupled elastic lattices have not yet been employed to create 1D topological insulators, with the exception of magnetically coupled spinners [39,40], a system that exhibits only rotational modes, thereby excluding the presence of

---
*taehwa.lee@toyota.com
†daraio@caltech.edu
‡These authors contributed equally to this work.

multimodal topological edge modes. In this context, multimodal topolgocal edge modes were studied for a 1D continuous elastic system [41]. The authors found longitudinal and bending topological edge modes, operating at vastly different frequencies, limiting their possibility of interaction. For the sake of completeness, we mention the presence of several other works on quasi-1D discrete elastic lattices with several DOFs per oscillators (see, e.g., Refs. [42,43]).

In this work, we use a quasi-1D lattice of repelling magnets, to demonstrate multimodal topological edge modes and to study the interplay between low-dimensional topological phases. We design the propagation properties of the lattice controlling the magnets' initial configuration and disorder. Our tunable system allows the control of energy distribution between longitudinal and transverse topological waves within a similar frequency range by varying the excitation frequency, actuator's angle of incidence, and the degree of lattice disorder.

## II. MODEL, RESULTS AND DISCUSSION

### A. Magnetoelastic lattice

The magnetoelastic lattice is composed of a 1D array of permanent magnets, each supported by circular elastic rods, as illustrated in Fig. 1(a). The array of magnets on rods is confined by fixed permanent magnets arranged at predefined distances along the array's boundaries. Such quasi-1D geometry, allows the lattice to support both longitudinal ($U$) and transverse ($V$) wave propagation [31]. In the periodic limit of the linear regime, the system can be represented by a discrete model, incorporating a series of masses connected by intercoupling, $k_{0,j}$, and intracoupling, $k_{1,j}$, springs, with $j = \{U, V\}$. The circular rods function as ground springs (stiffness $k_{g,j}$), while their positions ensure force equilibrium. We design the magnetoelastic lattice to uniquely exhibit equal ratios of alternating coupling strengths for longitudinal ($U$) and transverse ($V$) waves, i.e., $k_{0,U}/k_{1,U} = k_{0,V}/k_{1,V}$. As we show below, this choice leads to a mapping to the Su-Schrieffer-Heeger (SSH) lattice [44–46] for both the transverse and longitudinal directions. Thus, both $U$ and $V$ topological phases can be realized by introducing stronger intercoupling springs, relative to the (weaker) intracoupling springs ($k_{0,j} > k_{1,j}$), for a winding number of $w = 1$ as shown within the Supplemental Material [47]. Depending on the excitation frequency ($f_{UV,U,V}$) and angle ($\alpha$), our magnetoelastic lattice enables either the simultaneous excitation of topological modes or the selective excitation of either one of them, as illustrated in Fig. 1(b). As shown in Fig. 1(c), the proposed topological magnetoelastic lattice is experimentally constructed using ten magnets on rods, and the repulsive force is characterized as a function of the distance $d$ by a nonlinear relation, $F = Ad^p$, with experimentally obtained
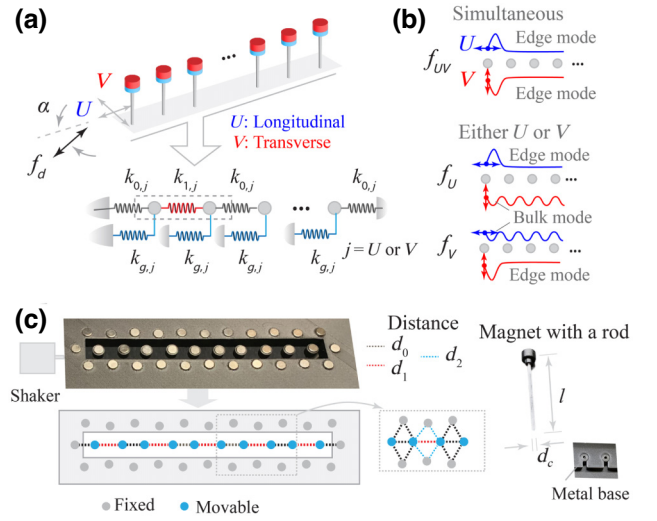


FIG. 1. Multimodal topological elastic lattices. (a) Elastic lattices composed of repulsive magnets supported by elastic rods for both longitudinal ($U$) and transverse ($V$) modes (excitation frequency $f_d$ and angle $\alpha$). The corresponding discrete model consists of a series of masses connected by ground springs ($k_g$) and coupling springs ($k_0$ and $k_1$). The two-magnet unit cell is indicated by a dashed rectangle. (b) Topological modes enabled by the magnetic lattice for simultaneous ($U$ and $V$) or selective ($U$ or $V$) topological modes. (c) Photo of the fabricated magnetic lattice and magnet-on-rod (diameter $d_c$ and length $l$). The distances between the magnets ($d_{0,1,2}$) are highlighted by different color codes. The angle between $d_1$ and $d_2$ is given by $\theta = 56°$.

$A = 2 \times 10^{-9}$ N/m$^p$ and $p = -4.1$ (see Fig. S1 within the Supplemental Material [47]).

### B. Equation of motion and dispersion relation

To determine the equations of motion for the movable magnets, we focus on the magnet with index $n \in \mathbb{Z}$ whose dynamics is dictated by Newton's second law [47]

$$m\ddot{\mathbf{X}}_n = \mathbf{F}_c^n + \mathbf{F}_\gamma^n + \mathbf{F}_\epsilon^n + \sum_{s=1}^{6} \mathbf{F}_s^n, \quad (1)$$

where $m$ and $\mathbf{X}_n = (u_n, v_n)$ represent the constant mass and the displacement of the magnet with index $n$ from its equilibrium position. Further, $\mathbf{F}_s^n$ ($s = 1$ to 6) denotes the force describing the magnetic interaction between the magnet at site $n$ and its $s$th nearest neighbor [see Fig. 1(c)]. In addition, $\mathbf{F}_c^n$ and $\mathbf{F}_\gamma^n$ denote the onsite and damping forces, which, respectively, are described by the rod elastic stiffness ($k_c$) and damping coefficient ($\gamma$). Moreover, $\mathbf{F}_\epsilon^n$ represents the (random) resultant forces at site $n$, emerging from all imperfections present in the base-rod-magnet apparatus. We assume that $\mathbf{F}_\epsilon^n = -\mathbf{K}_c\mathbf{E}_n$, with $\mathbf{E}_n = (\epsilon_{u,n}, \epsilon_{v,n})$ being a 2D disorder parameter drawn from the interval $[-W/2, W/2] \times [-W/2, W/2]$ with a uniform probability distribution.

In the linear regime ($\|\mathbf{X}_n - \mathbf{X}_{n+1}\|/a \ll 1$), the periodic ($W = 0$) and lossless ($\gamma = 0$) lattice simplifies Eq. (1) to a linear form, allowing for the eigenvalue analysis of the system [47]. Assuming a diatomic unit cell with index $s$, we denote the displacements of its left ($L$) and right ($R$) magnets $u_{L(R)}^s = U_{L(R)} e^{-i(\omega t - ksa)}$ and $v_{L(R)}^s = V_{L(R)} e^{-i(\omega t - ksa)}$ with $\omega$ being the radian frequency, $k$ the wave number, and $a = d_0 + d_1$ the cell's dimension. It follows that,

$$m\omega^2 \Psi = \mathbf{H}\Psi, \quad \text{with } \mathbf{H} = \begin{pmatrix} \mathbf{H}_U & \mathbf{0} \\ \mathbf{0} & \mathbf{H}_V \end{pmatrix}, \quad (2)$$

and $\Psi$, a column matrix with entries $(U_L, U_R, V_L, V_R)$. Clearly the longitudinal and transverse waves are uncoupled, encoded within $\mathbf{H}$ from its block-diagonal construction in which

$$\mathbf{H}_j = \begin{pmatrix} k_{t,j} & -k_{1,j} - k_{0,j} e^{-ika} \\ -k_{1,j} - k_{0,j} e^{ika} & k_{t,j} \end{pmatrix}, \quad (3)$$

with $k_{t,j} = k_{0,j} + k_{1,j} + k_{g,j}$. Note that each submatrix $\mathbf{H}_j$, after the removal of the constant diagonal, possesses chiral symmetry, i.e., $[\mathbf{H}_j - k_{t,j}\mathbf{I}]\sigma_z + \sigma_z[\mathbf{H}_j - k_{t,j}\mathbf{I}] = 0$ with $\mathbf{I}$ being the identity matrix and $\sigma_z = \begin{pmatrix} 1 & 0 \\ 0 & -1 \end{pmatrix}$ the chiral operator. Consequently, $\mathbf{H}_j$ can be mapped to the SSH lattice [44,49].

The longitudinal coupling in a linear regime is given by $k_{0(1),U} = -Ap|d_{0(1)}|^{p-1}$, which has a greater magnitude than the transverse coupling $k_{0(1),V} = -A|d_{0(1)}|^{p-1}$. It is worth noting that, the fixed surrounding magnets also contribute to an added stiffness to the ground spring, i.e., $k_{g,j} = k_c + k_{\text{fix},j}$ [47]. Interestingly, the transverse ground stiffness exceeds the longitudinal one due to $k_{\text{fix},j}$ varying in both $U$ and $V$ directions. The large ground stiffness along the transverse direction can compensate the smaller coupling stiffness $k_{0(1),V} = k_{0(1),U}/|p|$ for similar total stiffness (i.e., $k_{t,U} \approx k_{t,V}$), permitting $U$ and $V$ waves to coexist in a similar frequency range. The dispersion relation of the $U$ and $V$ waves is expressed by

$$\omega_j^2 = \frac{k_{t,j} \pm \sqrt{k_{0,j}^2 + k_{1,j}^2 + 2k_{0,j}k_{1,j}\cos(ka)}}{m}. \quad (4)$$

The linear dispersion relation of the elastic lattice is calculated by performing a 2D fast Fourier transform (2DFFT) on the displacement fields at moderate excitation, obtained for an excitation angle of $\alpha = 15°$, as shown in Figs. 2(a) and 2(b) for experiment and simulation, respectively. In experiments, the magnet with index $n = 1$ is excited by applying monochromatic sine waves at frequency $f_d$ (see further experimental details [47]). The experimental results show excellent agreement with
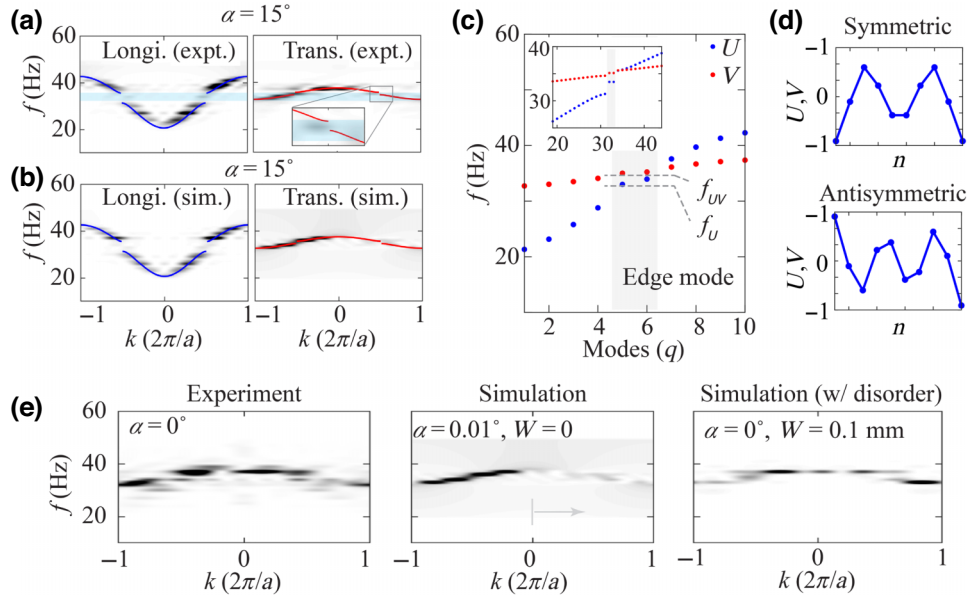


FIG. 2. Dispersion relation of the topological magnetoelastic lattices. (a) Experimental and (b) numerical dispersion relations for the (left) longitudinal and (right) transverse waves. The solid blue and red curves indicate the analytical results obtained for a bulk chain [Eq. (4)] with band gaps highlighted using light blue strips. (c) Frequency against mode index for a chain of 10 and (inset) 64 magnets obtained using numerical diagonalization [48]. The frequencies of topological modes are highlighted by the gray shaded areas. (d) Displacement profiles corresponding to the topological symmetric (S) and antisymmetric (AS) modes. (e) Effect of unintended imperfections on experimental measurements. (Left) Experimentally obtained transverse dispersion relation ($\alpha \approx 0°$) and corresponding simulation results using (middle) a small misalignment of the driver ($\alpha = 0.01°$ and $W = 0$), and (right) weak disorder ($\alpha = 0°$, $W = 0.1$ mm).

numerical simulations performed using direct numerical integration [50–52] of Eq. (1) (with $W = 0$ mm and $\gamma = 2.15 \times 10^{-3}$ Ns/m) as well as with the analytical dispersion relation of the linearized model [Eq. (4)] [Figs. 2(a) and 2(b), solid lines]. Remarkably, topological bandgaps are observed for both longitudinal and transverse waves, occurring in a similar frequency range (light blue shade).

The numerical diagonalization of the eigenvalue problem [Eq. (2)] associated to a finite chain of $N = 10$ magnets clearly shows two topological modes [Fig. 2(c), highlighted by a gray shaded region] within the band gap for the $U$ (respectively, $V$) direction, corresponding to symmetric ($S$) and antisymmetric ($AS$) modes, as shown in Fig. 2(d). Intriguingly, the finite size enables the upper $U$ and lower $V$ topological modes to closely align and be simultaneously excited at the same driving frequency, whereas, in the inset of Fig. 2(c), a longer chain ($N = 64$) shows decreased frequency proximity due to weaker modal hybridization (stemming from smaller evanescent coupling of localized modes at chain ends). By tuning the zigzag arrangement of the fixed magnets ($k_{0,j} \gg k_{1,j}$), we can control the frequency overlap of both $U$ and $V$ topological edge modes, realizing the "complete" overlap for a chain of $N = 10$ ($N = 64$) magnets [47].

Our experimental magnetoelastic lattice unavoidably exhibits unintended disorder. This is evidenced by both backward and forward traveling transverse waves appearing during excitation by purely longitudinal signals ($\alpha \approx 0°$), as shown in the left panel of Fig. 2(e). If the excitation aligns directly with the perfectly straight lattice, it induces purely longitudinal motion without a transverse one. This behavior is observed for the lattice maintaining a straight-line configuration, ensuring lateral symmetry. This suggests that the disorder causes the conversion of longitudinal waves into transverse ones due to symmetry breaking. Numerical simulations show that transverse waves can be caused by small misalignment (middle), which does not fully explain the observed back-scattered waves in experiments. However, introducing weak disorder ($W = 0.1$ mm [53]) into simulations allows for better agreement between numerical findings and experimental observations (right).

## C. Topological edge modes and pseudospin observation

We also study the topological modes by looking at the dynamical properties of our chain of magnets. In Fig. 3(a), we show space-time diagrams of the longitudinal displacements ($|u_n(t)|$), for $f_d = 34$ Hz (respectively, 33.48 Hz) generated through experiments (respectively, simulations). In simulations, we set $W = 0$ mm (no disorder). The colormaps highlight reduced displacements for magnets $n = 2, 5, 7, 9$, featured in the shapes of the topological $S$ and $AS$ modes. The relative driving frequency mismatch $\propto 1\%$, between the experiments and numerical simulations is negligible and can be attributed to the fact that, in simulations, we can model smaller frequency step size. Nonetheless, the presence of imperfections can also contribute into shifting the frequency spectrum (e.g., Ref. [47, Fig. S10]).

The magnified space-time diagrams of $u_n(t)$ from experimental (respectively, numerical) data are plotted for three different driving frequencies $f_d = 33, 34,$ and 35 Hz
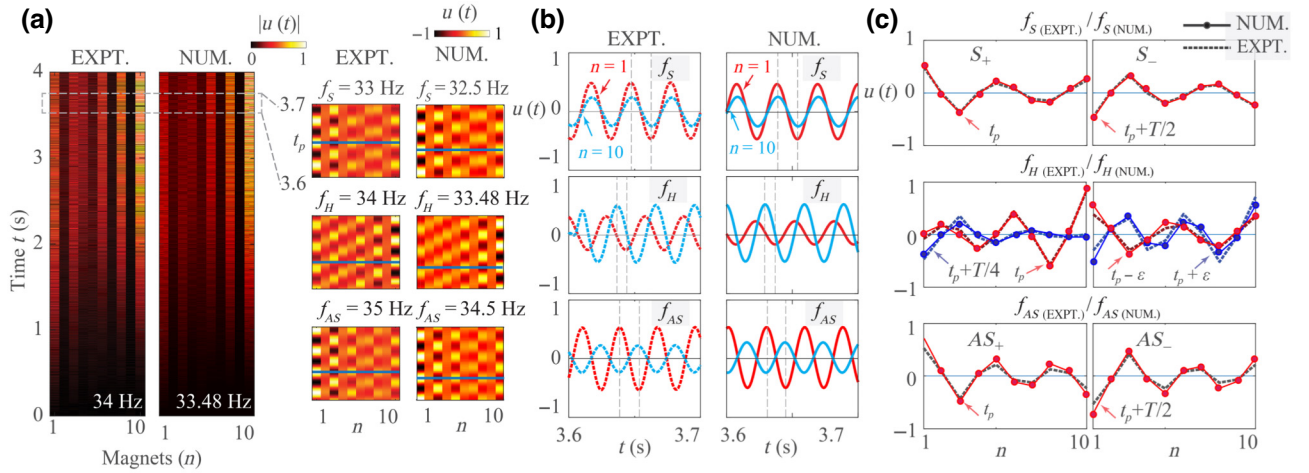


FIG. 3. Observation of topological edge modes for longitudinal excitation ($\alpha = 0°$). (a) The rescaled absolute displacements ($|u_n(t)|$) in space ($n$) and time ($t$) from experimental (respectively, numerical) data with $f_d = 34$ Hz (respectively, $f_d = 33.48$ Hz). The $u_n(t)$ in the time window $t \in [3.6, 3.7]$ from experimental (respectively, numerical) data, are plotted for three $f_d$: $f_S$ (top), $f_H$ (middle), and $f_{AS}$ (bottom). (b) The displacements $u_n(t)$ against $t$ for the magnets with indices $n = 1$ (red) and $n = 10$ (blue) obtained at $f_S$, $f_H$, and $f_{AS}$. (c) Instant displacement profiles at times $t_p$ and $t_p + \Delta$ ($\Delta = \{T/2, T/4\}$, $T = 1/f_d$) indicated by the vertical dashed lines in (b), and times $t_p \pm \epsilon$ with $\epsilon = T/5$: symmetry (top) for $f_d = f_S$; antisymmetry (bottom) for $f_d = f_{AS}$; for $f_d = f_H$, hybrid (middle left) at $t_p$, $t_p + \Delta$ and antisymmetry (middle right) at $t_p + \epsilon$ and symmetry (middle right) at $t_p - \epsilon$.

(respectively, $f_d = 32.5$, 33.48, and 34.5 Hz) in the gap of the longitudinal frequency band. We clearly observe distinct patterns. More specifically, in Fig. 3(b), we examine $u_n(t)$ for the magnets with indices $n = 1$ and 10, whose experimental data are (tenfold) upsampled using advanced interpolating algorithm for clarity. An in-phase motion of the two magnets ($n = 1$ and 10) is observed for $f_S = 33$ Hz (respectively, 32.5 Hz), corresponding to symmetric displacement profiles at instants $t_p$ and $t_p + T/2$ [dashed lines in the top panels of Fig. 3(b)], see $S_\pm$ in Fig. 3(c). Meanwhile, the end magnets exhibit an out-of-phase motion at the similar instants as above for the case $f_{AS} = 35$ Hz (respectively, 34.5 Hz) as antisymmetric displacement profiles, as shown by the $AS_\pm$ in Fig. 3(c). Note that there is a minor disruption of the mirror (point) symmetric profiles for $S_\pm$ ($AS_\pm$) due to the presence of the driver at the position of the first magnet.

Notably, for the intermediate driving frequency, $f_H = 34$ Hz (respectively, 33.48 Hz), we find from the middle panel of Fig. 3(b), the displacements of the magnets with indices $n = 1$ and $n = 10$ are neither in-phase nor out-of-phase. We instead find oscillations between left- and right-localized states originating from the presence and excitation of both $S$ and $AS$ topological modes. These oscillations have also been studied recently in the context of photonic SSH lattices [54]. Their dynamics become evident when capturing the snapshots of $u_n(t)$ at times $t_p$ and $t_p + T/4$, whenever the amplitudes of the end magnets vanishes [middle-left panel of Fig. 3(c)]. Further they are dynamically connected via the $S_\pm$ and $AS_\pm$ topological modes captured at instants $t_p \pm \epsilon$ ($\epsilon = T/5$), see middle-right panel of Fig. 3(c).

It is worth commenting a bit more the middle panel of Fig. 3(b), which also depict larger displacements for the magnet with index $n = 10$ compared to the one with $n = 1$, where the driver is located. In fact, our swiping frequency step of 1 Hz, is not sufficient to perfectly balance the energy distribution between the $S$ and $AS$ modes. This energy imbalance leads to the magnitude of the displacements of the right localized states to be larger when compared to its left counterpart as shown in the middle-left panel of Fig. 3(c), assuming both states are superimposed. Consequently, the displacements of the driver at position $n = 1$ is, in general, smaller than the one of the last magnet of the chain with index $n = 10$.

Furthermore, we also observe the circulation of displacement profiles: $S_+ \xrightarrow{T/4} AS_- \xrightarrow{T/4} S_- \xrightarrow{T/4} AS_+$, through which the combination $S \pm AS$ giving rise to the hybrid states emerges at an intermediate time step. It follows that the displacement profile of the system can be represented by $\mathbf{u}(t) = \cos(2\pi t/T)S - \sin(2\pi t/T)AS$ with basis $S/AS$ (spin$-$: $S - iAS$), emulating a pseudo (Fermi-like) spin through modal hybridization [55], as shown in Fig. 4(a). In addition, its circulation (spin
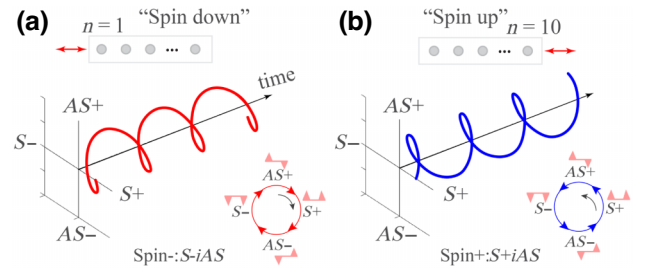


FIG. 4. Pseudospin observation by topological modes. The pseudospin direction is controlled by the excitation: (a) pseudospin down for the left-end excitation ($n = 1$) and (b) pseudospin up for the right-end excitation ($n = 10$).

direction) can be inverted in our mechanical lattice, e.g., by exciting the other end of the chain (spin+: $S + iAS$) [Fig. 4(b)], see Ref. [47, Fig. S18]. A striking proposition of our work is that such pseudospin states can independently coexist along both $U$ and $V$ directions. Unlike typical 2D structures, in our compact quasi-1D setup, these are nonpropagating pinned states.

### D. Multimodal topological edge modes

We experimentally demonstrate the control of multimodal topological modes using $f_d$ as a tuning knob, for $\alpha = 15°$. In Fig. 5(a), the simultaneous excitation of the longitudinal $AS$ and transverse hybrid topological edge modes is observed for $f_d = 35$ Hz. This $f_d$ falls within the band gaps of both longitudinal and transverse dispersion relations. Interestingly, these two simultaneously excited topological modes exhibit complete spatial overlap, in contrast to other similar topological mechanical systems for which certain DOFs per unit oscillator remain dependent in their linearized limit [43].

In addition, at driving frequency $f_d = 34$ Hz, within the longitudinal band gap but outside the transverse band gap, we demonstrate the selective excitation of the longitudinal topological (hybrid) edge modes along with a transverse bulk mode, as seen in Fig. 5(b). The upper panels of Figs. 5(a) and 5(b) show the real space trajectories (rescaled by a factor of 40) of the magnets, which highlight an elliptical motion oriented along $\theta_r \approx 30°$ (for the magnets with odd indices) with respect to the longitudinal direction. Video 1 shows the corresponding magnet motions for 34 Hz. The orientation is related to the phase delay ($\delta$) between the $U$ and $V$ waves when parameterized like Lissajous curve, leading to $\delta \approx -\pi/4$.

### E. Effect of disorder

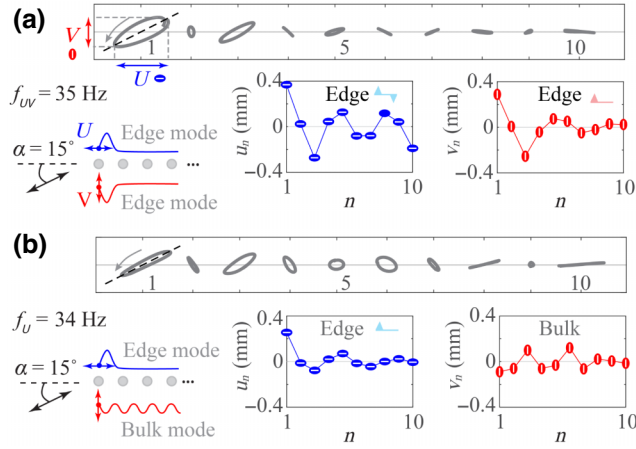Lets us now study the effects of disorder in our quasi-1D model of Fig. 1. In this context, the eigenvalue problem

FIG. 5.   Control of multimodal topological edge modes. (a) Simultaneous excitation of both longitudinal ($U$) and transverse ($V$) topological modes for an excitation frequency of $f_d = 35$ Hz with $\alpha = 15°$. (b) Selective excitation of the $U$ mode for $f_d = 34$ Hz and $\alpha = 15°$. In upper panels of (a),(b), the real space trajectories (rescaled by a factor of 40) of the magnets are also displayed.

becomes

$$m\omega^2\Psi = \mathbf{H}\Psi, \quad \text{with } \mathbf{H} = \begin{pmatrix} \mathbf{H}_U & \mathbf{H}_{UV} \\ \mathbf{H}_{VU} & \mathbf{H}_V \end{pmatrix}, \quad (5)$$

where $\Psi$ is now a $2N$ displacement vector with components $U_{L,s}$, $U_{R,s}$, $V_{L,s}$, $V_{R,s}$ for the cell with index $s$. Consequently, the Hamiltonian matrix, $\mathbf{H}$ is made up of four random block tridiagonal matrices $\mathbf{H}_U$, $\mathbf{H}_V$, $\mathbf{H}_{UV}$, and $\mathbf{H}_{VU}$ of rank $N$ (see Supplemental Material [47] for details). Further, the $\mathbf{H}_{UV}$ and $\mathbf{H}_{VU}$ induces the coupling between the $U$ and $V$ DOFs. As such, each wave in the system possesses both $U$ and $V$ DOFs, in a way that a random realization of disorder leads to a random tailoring of the energy distribution between the $U$ and $V$ waves. It is worth pointing out that the resulting random matrix $\mathbf{H}$ does not respect the chiral symmetry as usually found in the case of the SSH model.
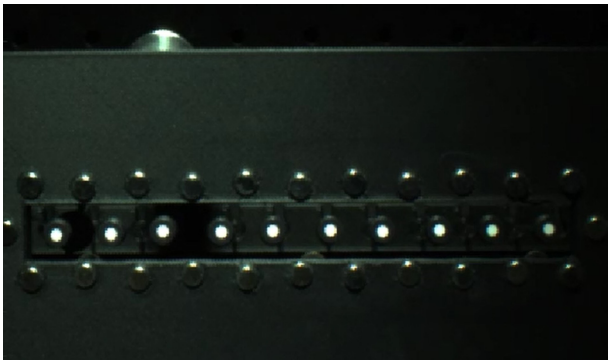


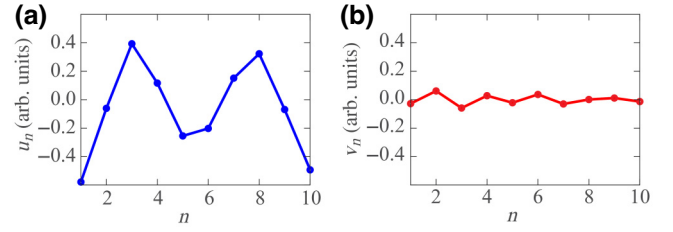VIDEO 1.   High-speed imaging of the magnet motions for 34 Hz.



FIG. 6.   Normal-mode analysis. The system is made up of $N = 10$ movable magnets on the geometric configuration obtained using $d_0 = 15$ mm, $\theta = 56°$ (see Fig. 1) and $W = 1$ mm. (a) The longitudinal and (b) transverse displacements of the mode with wave number $q = 5$. This mode corresponds to the longitudinal topological $S$ mode in the periodic limit of $W = 0$ mm [see upper panel of Fig. 2(d)].

For $W = 1$ mm, we perform a normal-mode analysis on the system of Fig. 1(c) with $d_0 = 15$ mm, and $\theta = 56°$. Figure 6 shows the spatial profile of the longitudinal topological $S$ [Figs. 6(a) and 6(b)]. Clearly, the $S$ mode admits $U$ and $V$ displacements. Further, the symmetric shape of the $U$ displacements, seeing for $W = 0$ mm is altered in Fig. 6(a). The latter originates from the fact that a portion of the modes' spectral energy in the clean limit ($W = 0$ mm) has shifted toward the $V$ direction, Fig. 6(b). Similar observations can also be drawn for the longitudinal $AS$ mode [47]. Furthermore, in the Supplemental Material [47], we show that this phenomenon is robust whilst growing lattice size and explore additional dependence of the spectrum of the system toward disorder.

Despite the nonchiral nature of the disorder and its induced coupling between the DOFs, we proceed demonstrating that the topological modes in our lattice are robust, whilst the addition of weak strength of such disorder. The computation results of the winding number $w_j$, presented as a function of disorder strength $W$ along the longitudinal ($j = U$) and transverse ($j = V$) directions, are depicted in Figs. 7(a) and 7(b), respectively. Note that this analysis is performed for the system configuration (i.e., $d_0 = 15$ mm, and $\theta = 56°$), but choosing a longer chain of $N = 64$ moving magnets in order to mimic the thermodynamic limit. In addition, these winding numbers $w_j$ are obtained by averaging the the local topological marker (LTM) across ten cells at the center of the chain and over five realizations of disorder (see Refs. [46,56–59] for further details).

Clearly, for $W \to 0$ mm, the $w_j \to 1$, indicating topologically nontrivial phases along both $U$ and $V$ directions as expected. On the other hand, when $W \to 1$ mm, we see that the $w_j$ are decreasing. Nevertheless, for intermediate values of $W \in [0, 1]$ mm, the $w_j$ remains close to 1, which suggests the persistence of the topological phases along both $U$ and $V$ directions. Further in the Supplemental Material [47], we also show the band gaps remain open along both directions in this interval of $W$ values.
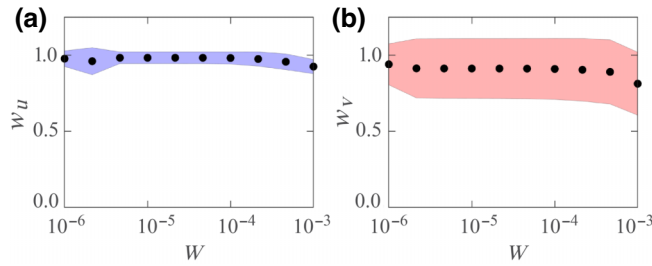
FIG. 7. Topological marker. (a) [(b)] Winding number of the system $w_U$ (respectively, $w_V$) along the longitudinal (respectively, transverse) direction against $W$. They are computing averaging a local topological marker across ten central cells over five disorder realizations of a lattice with $N = 64$ movable magnets. In addition, the geometrical parameters are fixed to $d_0 = 15$ mm and $\theta = 56°$. Note that the shaded areas represent one's standard deviation.

## III. CONCLUSION

We demonstrated control of longitudinal and transverse topological modes in a compact, magnetoelastic quasi-1D lattice. In the small amplitude regime, our system reduced to two superposed mechanical SSH models arranged perpendicularly, with tunable effective elastic coefficients. We showed that adjusting the excitation angle and frequency allows us to control longitudinal and transverse topological waves, with lattice disorder aiding energy conversion and highlighting system robustness. Our magnetoelastic lattice offers a platform to further explore interactions between topology, nonlinearity, and disorder, and serves as inspiration for wave-control applications, like in sensing and information processing.

## ACKNOWLEDGMENTS

[1] C. L. Kane and E. J. Mele, $Z_2$ topological order and the quantum spin Hall effect, Phys. Rev. Lett. **95**, 146802 (2005).

[2] D. Hsieh, D. Qian, L. Wray, Y. Xia, Y. S. Hor, R. J. Cava, and M. Z. Hasan, A topological Dirac insulator in a quantum spin Hall phase, Nature **452**, 970 (2008).

[3] P. St-Jean, V. Goblot, E. Galopin, A. Lemaître, T. Ozawa, L. Le Gratiet, I. Sagnes, J. Bloch, and A. Amo, Lasing in topological edge states of a one-dimensional lattice, Nat. Photonics **11**, 651 (2017).

[4] L. Lu, J. D. Joannopoulos, and M. Soljačić, Topological photonics, Nat. Photonics **8**, 821 (2014).

[5] C. He, X. Ni, H. Ge, X.-C. Sun, Y.-B. Chen, M.-H. Lu, X.-P. Liu, and Y.-F. Chen, Acoustic topological insulator

[6] and robust one-way sound transport, Nat. Phys. **12**, 1124 (2016).

[6] G. Ma, M. Xiao, and C. T. Chan, Topological phases in acoustic and mechanical systems, Nat. Rev. Phys. **1**, 281 (2019).

[7] M. Lohse, C. Schweizer, H. M. Price, O. Zilberberg, and I. Bloch, Exploring 4D quantum Hall physics with a 2D topological charge pump, Nature **553**, 55 (2018).

[8] O. Zilberberg, S. Huang, J. Guglielmon, M. Wang, K. P. Chen, Y. E. Kraus, and M. C. Rechtsman, Photonic topological boundary pumping as a probe of 4D quantum Hall physics, Nature **553**, 59 (2018).

[9] L. Yuan, Q. Lin, M. Xiao, and S. Fan, Synthetic dimension in photonics, Optica **5**, 1396 (2018).

[10] A. Dutt, M. Minkov, I. A. Williamson, and S. Fan, Higher-order topological insulators in synthetic dimensions, Light Sci. Appl. **9**, 131 (2020).

[11] R. Citro and M. Aidelsburger, Thouless pumping and topology, Nat. Rev. Phys. **5**, 87 (2023).

[12] X. Ni, K. Chen, M. Weiner, D. J. Apigo, C. Prodan, A. Alu, E. Prodan, and A. B. Khanikaev, Observation of Hofstadter butterfly and topological edge states in reconfigurable quasi-periodic acoustic crystals, Commun. Phys. **2**, 55 (2019).

[13] H. Chen, H. Zhang, Q. Wu, Y. Huang, H. Nguyen, E. Prodan, X. Zhou, and G. Huang, Creating synthetic spaces for higher-order topological sound transport, Nat. Commun. **12**, 5028 (2021).

[14] Z.-G. Chen, W. Zhu, Y. Tan, L. Wang, and G. Ma, Acoustic realization of a four-dimensional higher-order Chern insulator and boundary-modes engineering, Phys. Rev. X **11**, 011016 (2021).

[15] Z. Zhang, Y. Tian, Y. Cheng, Q. Wei, X. Liu, and J. Christensen, Topological acoustic delay line, Phys. Rev. Appl. **9**, 034032 (2018).

[16] S. Li, D. Zhao, H. Niu, X. Zhu, and J. Zang, Observation of elastic topological states in soft materials, Nat. Commun. **9**, 1 (2018).

[17] N. Boechler, G. Theocharis, and C. Daraio, Bifurcation-based acoustic switching and rectification, Nat. Mater. **10**, 665 (2011).

[18] B. Deng, P. Wang, Q. He, V. Tournat, and K. Bertoldi, Metamaterials with amplitude gaps for elastic solitons, Nat. Commun. **9**, 1 (2018).

[19] D. Smirnova, D. Leykam, Y. Chong, and Y. Kivshar, Nonlinear topological photonics, Appl. Phys. Rev. **7**, 021306 (2020).

[20] M. S. Kirsch, Y. Zhang, M. Kremer, L. J. Maczewsky, S. K. Ivanov, Y. V. Kartashov, L. Torner, D. Bauer, A. Szameit, and M. Heinrich, Nonlinear second-order photonic topological insulators, Nat. Phys. **17**, 995 (2021).

[21] F. Zangeneh-Nejad and R. Fleury, Nonlinear second-order topological insulators, Phys. Rev. Lett. **123**, 053902 (2019).

[22] R. Chaunsali and G. Theocharis, Self-induced topological transition in phononic crystals by nonlinearity management, Phys. Rev. B **100**, 014302 (2019).

[23] R. Chaunsali, H. Xu, J. Yang, P. G. Kevrekidis, and G. Theocharis, Stability of topological edge states under strong nonlinear effects, Phys. Rev. B **103**, 024106 (2021).

[24] R. K. Pal, J. Vila, M. Leamy, and M. Ruzzene, Amplitude-dependent topological edge states in nonlinear phononic lattices, Phys. Rev. E **97,** 032209 (2018).

[25] M. I. Rosa, M. J. Leamy, and M. Ruzzene, Amplitude-dependent edge states and discrete breathers in non-linear modulated phononic lattices, ArXiv:2201.05526 (2022).

[26] A. Darabi and M. J. Leamy, Tunable nonlinear topological insulator for acoustic waves, Phys. Rev. Appl. **12,** 044030 (2019).

[27] C. Chong, Y. Wang, D. Maréchal, E. G. Charalampidis, M. Molerón, A. J. Martínez, M. A. Porter, P. G. Kevrekidis, and C. Daraio, Nonlinear localized modes in two-dimensional hexagonally-packed magnetic lattices, New J. Phys. **23,** 043008 (2021).

[28] W. Jiao and S. Gonella, Nonlinear harmonic generation in two-dimensional lattices of repulsive magnets, Phys. Rev. E **103,** 012213 (2021).

[29] C. Chong, A. Foehr, E. G. Charalampidis, P. G. Kevrekidis, and C. Daraio, Breathers and other time-periodic solutions in an array of cantilevers decorated with magnets, Math. Eng. **1,** 489 (2019).

[30] M. Molerón, C. Chong, A. J. Martínez, M. A. Porter, P. G. Kevrekidis, and C. Daraio, Nonlinear excitations in magnetic lattices with long-range interactions, New J. Phys. **21,** 063032 (2019).

[31] A. A. Watkins and O. R. Bilal, Demultiplexing infrasound phonons with tunable magnetic lattices, Front. Mater. **7,** 1 (2020).

[32] F. Allein, V. Tournat, V. E. Gusev, and G. Theocharis, Tunable magneto-granular phononic crystals, Appl. Phys. Lett. **108,** 161903 (2016).

[33] M. Hwang and A. F. Arrieta, Input-independent energy harvesting in bistable lattices from transition waves, Sci. Rep. **8,** 3630 (2018).

[34] Y. Wang, B. Yousefzadeh, H. Chen, H. Nassar, G. Huang, and C. Daraio, Observation of nonreciprocal wave propagation in a dynamic phononic lattice, Phys. Rev. Lett. **121,** 194301 (2018).

[35] K. H. Matlack, M. Serra-Garcia, A. Palermo, S. D. Huber, and C. Daraio, Designing perturbative metamaterials from discrete models, Nat. Mater. **17,** 323 (2018).

[36] E. Norouzi, A. A. Watkins, and O. R. Bilal, Classification of emerging patterns in self-assembled two-dimensional magnetic lattices, Phys. Rev. E **104,** 044902 (2021).

[37] A. A. Watkins, A. Eichelberg, and O. R. Bilal, Exploiting localized transition waves to tune sound propagation in soft materials, Phys. Rev. B **104,** L140101 (2021).

[38] A. Eichelberg, A. A. Watkins, and O. R. Bilal, Metamaterials with reprogrammable reciprocity, Phys. Rev. Appl. **18,** 054049 (2022).

[39] D. J. Apigo, K. Qian, C. Prodan, and E. Prodan, Topological edge modes by smart patterning, Phys. Rev. Mater. **2,** 124203 (2018).

[40] J. Vila, G. H. Paulino, and M. Ruzzene, Role of nonlinearities in topological protection: Testing magnetically coupled fidget spinners, Phys. Rev. B **99,** 125116 (2019).

[41] J. Yin, M. Ruzzene, J. Wen, D. Yu, L. Cai, and L. Yue, Band transition and topological interface modes in 1D elastic phononic crystals, Sci. Rep. **8,** 6806 (2018).

[42] E. Prodan, K. Dobiszewski, A. Kanwal, J. Palmieri, and C. Prodan, Dynamical Majorana edge modes in a broad class of topological mechanical systems, Nat. Commun. **8,** 14587 (2017).

[43] F. Allein, A. Anastasiadis, R. Chaunsali, I. Frankel, N. Boechler, F. K. Diakonos, and G. Theocharis, Strain topological metamaterials, Nat. Commun. **14,** 6633 (2023).

[44] W. P. Su, J. R. Schrieffer, and A. J. Heeger, Solitons in polyacetylene, Phys. Rev. Lett. **42,** 1698 (1979).

[45] R. Süsstrunk and S. D. Huber, Classification of topological phonons in linear mechanical metamaterials, Proc. Natl. Acad. Sci. **113,** E4767 (2016).

[46] X. Shi, I. Kiorpelidis, R. Chaunsali, V. Achilleos, G. Theocharis, and J. Yang, Disorder-induced topological phase transition in a one-dimensional mechanical system, Phys. Rev. Res. **3,** 033012 (2021).

[47] See Supplemental Material at http://link.aps.org/supplemental/10.1103/PhysRevApplied.21.024049 for additional experimental data, numerical simulations, and dependencies of the static and dynamic properties of the system.

[48] W. H. Press, S. A. Teukolsky, W. T. Vetterling, and B. P. Flannery, *Numerical Recipes in Fortran 90 the art of Parallel Scientific Computing* (Cambridge University Press, Cambridge, 1996).

[49] J. K. Asbóth, L. Oroszlány, and A. Pályi, *A Short Course on Topological Insulators* (Springer Cham, Switzerland, 2016).

[50] E. Hairer, S. P. Nørsett, and G. Wanner, *Solving Ordinary Differential Equations I. Nonstiff Problems*, Springer Series in Computational Mathematics (Springer, Berlin, 1993), 2nd ed, Vol. 14.

[51] C. Danieli, B. Many Manda, T. Mithun, and C. Skokos, Computational efficiency of numerical integration methods for the tangent dynamics of many-body Hamiltonian systems in one and two spatial dimensions, Math. Eng. **1,** 447 (2019).

[52] DOP853 codes freely available from, http://www.unige.ch/hairer/software.html.

[53] In this context, $W/a \ll 1$ with $a$ being the length of the unit cell of the chain of movable magnets in the system's real space.

[54] N. K. Efremidis, Topological photonic Su-Schrieffer-Heeger-type coupler, Phys. Rev. A **104,** 053531 (2021).

[55] S.-Y. Yu, C. He, Z. Wang, F.-K. Liu, X.-C. Sun, Z. Li, H.-Z. Lu, M.-H. Lu, X.-P. Liu, and Y.-F. Chen, Elastic pseudospin transport for integratable topological phononic circuits, Nat. Commun. **9,** 3072 (2018).

[56] R. Bianco and R. Resta, Mapping topological order in coordinate space, Phys. Rev. B **84,** 241106 (2011).

[57] R. Bianco and R. Resta, Orbital magnetization as a local property, Phys. Rev. Lett. **110,** 087202 (2013).

[58] I. Mondragon-Shem, T. L. Hughes, J. Song, and E. Prodan, Topological criticality in the chiral-symmetric AIII class at strong disorder, Phys. Rev. Lett. **113,** 046802 (2014).

[59] E. J. Meier, F. Alex An, A. Dauphin, M. Maffei, P. Massignan, T. L. Hughes, and B. Gadway, Observation of the topological Anderson insulator in disordered atomic wires, Science **362,** 929 (2018).

[60] Center for High Performance Computing (CHPC) of South Africa, https://www.chpc.ac.za/.